Comparison of Dynamic Behavior of Steam–Air and Steam–Steam Solid Oxide Electrolysis Cell

Dongkeun Lee[a], Young Sang Kim[b], Yonggyun Bac[d] and Jin Young Park[d]

[a] Korea Institute of Machinery & Materials, Daejeon, South Korea, keun5832@kimm.re.kr, CA
[b] Korea Institute of Machinery & Materials, Daejeon, South Korea, yskim@kimm.re.kr
[c] Korea Institute of Machinery & Materials, Daejeon, South Korea, ygbae@kimm.re.kr
[d] Korea Institute of Machinery & Materials, Daejeon, South Korea, zeragon@kimm.re.kr

Abstract:

Hydrogen is considered a key energy carrier for carbon-neutral energy systems, and its demand is rapidly increasing. High temperature steam electrolysis using solid oxide electrolysis cells (SOECs) is a promising technology due to its high electrical efficiency. However, the economic feasibility of SOEC systems is strongly affected by auxiliary power consumption, among which the air blower on the oxygen side represents a significant share. In conventional SOEC systems, air is supplied to the oxygen electrode to remove produced oxygen and control the temperature, leading to substantial parasitic power consumption. Alternatively, supplying steam to the oxygen side enables oxygen removal while potentially reducing auxiliary power, as liquid water pumping requires considerably less energy than gas compression. In this study, the dynamic behavior of Steam–Air and Steam–Steam SOEC configurations is comparatively investigated. A dynamic SOEC model is developed to analyze transient system behavior, including temperature and current density responses. The dynamic characteristics of both configurations are compared at endothermic, thermoneutral, and exothermic operating conditions during load variations.

Keywords:

Solid oxide electrolysis cell; Steam sweep gas; Dynamic model; Simulation.

1. Introduction

Achieving carbon neutrality has become a central challenge of this century as the impacts of climate change intensify and the reliance on fossil fuels must be replaced by sustainable alternatives. Renewable energy sources such as solar and wind continue to grow rapidly, reaching record deployment levels in 2024 [1]. However, the intermittent and weather dependent nature of these resources creates a persistent mismatch between generation and demand, making large scale energy storage indispensable. Hydrogen is widely recognized as one of the most promising energy carriers for this purpose, offering zero emission combustion, high energy density, and versatility across industrial, transportation, and power sectors [1,2]. Unlike battery storage, hydrogen enables seasonal storage and long distance transport, making it an essential component of future net zero energy systems.

Among hydrogen production methods, high temperature water electrolysis using solid oxide electrolysis cells (SOECs) offers distinct thermodynamic advantages. SOEC operates at 700–900°C, where the electrical energy required for water splitting is partially replaced by thermal energy, enabling system efficiencies exceeding 90% on a higher heating value (HHV) basis [7]. This arises from the favorable thermodynamics at high temperatures, where the Gibbs free energy of the reaction decreases while the total enthalpy demand remains nearly constant [8]. The technology can utilize waste heat from industrial processes or nuclear power plants as the thermal input, further improving the overall system performance [2,7].

Despite its thermodynamic merits, the economic competitiveness of SOEC systems is strongly affected by auxiliary power consumption in the balance of plant (BoP) [2]. In conventional SOEC configurations, air is supplied to the oxygen electrode to remove the produced oxygen and to control the stack temperature. The air blower required for this function constitutes a significant portion of the total system auxiliary power. Min et al. [5] showed that at elevated operating pressures, the parasitic power of the air blower can grow substantially at 5 atm, blower power increases from less than 50 W to over 1,900 W against a stack power of approximately 4,600 W, accounting for more than 40% of the gross power demand. Saeedmanesh et al. [6] incorporated a dynamic air blower model into a 300kW SOEC system and demonstrated that the blower must operate

continuously to maintain oxygen removal and thermal control throughout transient operation. Reducing or eliminating the air blower therefore represents a meaningful opportunity for efficiency improvement and cost reduction.

An alternative strategy is to supply steam, rather than air, to the oxygen electrode as a sweep gas. Since steam is already available within the SOEC system for hydrogen production at the fuel electrode, no additional gas infrastructure is required on the oxygen side. More importantly, liquid water pumping requires orders of magnitude less energy than gas phase compression, which can substantially reduce parasitic power consumption. Barelli et al. [4] provided the first experimental demonstration of this concept, operating a single SOE cell with steam as the oxygen electrode sweep gas and confirming 100% pure oxygen production on a dry basis with negligible performance degradation compared to air sweep. Sun et al. [3] further investigated a reversible solid oxide cell system using steam as the anode sweep gas in electrolysis mode and reported an 8% increase in system efficiency and a 50% increase in total H2 production relative to the conventional air sweep configuration. Oxygen collected as a by product retains high purity because steam can be easily separated by condensation. Despite these encouraging results, the comparative dynamic behavior of Steam–Air and Steam–Steam SOEC configurations under transient operating conditions has not yet been investigated, which is essential for assessing practical feasibility and developing appropriate control strategies.

In this study, a dynamic SOEC model is developed to compare the transient behavior of the conventional Steam–Air configuration and the Steam–Steam configuration. Temperature and current density responses are analyzed during load variations across endothermic, thermoneutral, and exothermic operating conditions. Through this comparative analysis, the influence of the oxygen electrode sweep gas strategy on the dynamic behavior of the SOEC system is clarified, providing a basis for control strategy development and system level integration of the Steam–Steam configuration.

2. Model Development

2.1. Steam sweep gas SOEC

In this study, SOEC operating with steam as the sweep gas on the oxygen electrode (anode) side is modeled and compared against the conventional air sweep configuration. Fig. 1 shows a schematic of the Steam–Steam SOEC unit cell. The cell consists of a positive-electrolyte-negative (PEN) structure comprising a cathode electrode, a dense oxygen ion conducting electrolyte, and an anode electrode. H_2O and H_2 are supplied to the cathode channel, where steam is electrochemically reduced to produce hydrogen and oxygen ions (O^{2-}). The oxygen ions are conducted through the electrolyte to the anode, where they are oxidized to release O_2. In the Steam–Steam configuration, steam is supplied to the anode channel as a sweep gas, removing the produced O_2 and controlling the local oxygen partial pressure. The anode outlet therefore consists of a mixture of H_2O and O_2, from which pure oxygen can be recovered by simple steam condensation. The electrochemical half reactions at each electrode and the overall cell reaction are summarized in Table 1.

Table 1. *Electrochemical reaction of SOEC.*

Electrode	Reaction
Cathode	$O^{2-} \rightarrow \frac{1}{2}O_2 + 2e^-$
Anode	$H_2O + 2e^- \rightarrow H_2 + O^{2-}$
Overall	$H_2O \rightarrow H_2 + \frac{1}{2}O_2$

Schematic of the Steam–Steam SOEC unit cell model. Steam is supplied to both cathode and anode channels. The cathode channel carries H_2O and H_2, with the outlet stream of H_2O + H_2. The anode channel carries H_2O as sweep gas, with the outlet stream of H_2O + O_2. Oxygen ions (O^{2-}) produced at the cathode electrode are conducted through the electrolyte and oxidized at the anode electrode.

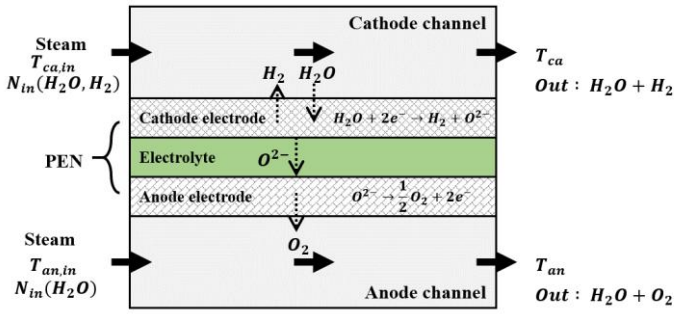

Figure. 1. *SOEC with steam sweep gas*

The dynamic model developed in this study is based on the model presented in a previous conference publication [1], and only a brief description is provided here. The model is organized as a segmented two-dimensional (2D) stack model and includes mass conservation, energy conservation, and electrochemical governing equations for each control volume. The key distinction from the model in [1] is the addition of the Steam–Steam anode configuration, which introduces a different set of anode mass conservation equations compared to the conventional air sweep case.

The mass conservation equation states that the rate of change of molar content in each control volume equals the net molar flow in minus flow out, adjusted for electrochemical consumption or production. For the cathode channel, where steam is consumed and hydrogen is produced:

$$\dot{N_{cat}} = \dot{C}_{cat} V_{cat} = N_{in,cat} - N_{out,cat} - reactions_{cat}$$

$$\dot{N_{H_2}} = N_{in,H_2} - N_{out,H_2} + \frac{j}{2F} A_{cat}$$

$$\dot{N_{H_2O}} = N_{in,H_2O} - N_{out,H_2O} - \frac{j}{2F} A_{cat}$$

The anode mass conservation equations differ between the two configurations studied. In the Steam–Air configuration, both N_2 and O_2 are present in the anode channel:

$$\dot{N_{N_2}} = N_{in,N_2} - N_{out,N_2}$$

$$\dot{N_{O_2}} = N_{in,O_2} - N_{out,O_2} + \frac{j}{4F} A_{an}$$

In the Steam–Steam configuration, only H_2O and O_2 are present in the anode channel, as no nitrogen is supplied:

$$\dot{N_{H_2O}} = N_{in,H_2O} - N_{out,H_2O}$$

$$\dot{N_{O_2}} = -N_{out,O_2} + \frac{j}{4F} A_{an}$$

where j is the local current density [A/cm^2], F is the Faraday constant [C/mol], and A_{cat}, A_{an} are the active areas of the cathode and anode segments [m^2], respectively.

The energy conservation equation for each gas channel control volume is formulated in terms of the enthalpy flow in and out of the control volume, heat transfer with the solid cell, and the heat of electrochemical reaction. For the cathode channel:

$$\dot{E} = \frac{d}{dt} \sum_{cat} N_{cat} e_{cat} = \left(q_{in,cat} - q_{out,cat}\right) + k_{c,sol}(T_{sol} - T_c) A_{cat} + r_{Red}\left[e_{H_2}(T_{sol}) - e_{H_2O}(T_{cat})\right] A_{cat}$$

where $k_{c,sol}$ is the convective heat transfer coefficient between the gas and cell [W/m^{2}K], T_{sol} and T_c are the cell and cathode gas temperatures [K], r_{Red} is the electrochemical reaction rate per unit area [mol/m^{2}s], and e_{H2}, e_{H2O} are the specific enthalpies of H_2 and H_2O [J/mol]. The same form is applied to the anode channel, with the appropriate species and boundary conditions for each configuration.

The cell voltage is calculated as the reversible potential plus the sum of overpotentials arising from activation, ohmic, and concentration losses:

$$U = U^{rev} + \eta_{Ohm} + \eta_{conc,\,cathode} + \eta_{conc,\,anode} + \eta_{act,\,cathode} + \eta_{act,\,anode}$$

The reversible potential is computed from the Nernst equation as a function of local gas composition and temperature. Each overpotential is evaluated using the local current density, temperature, and species concentrations. Detailed expressions for each term are given in [1].

The SOEC stack model is structured as a segmented 2D model in which each cell is discretized spatially along the flow direction. The governing equations described in sections are solved independently at each segment, allowing the spatial distributions of cell temperature and current density to be resolved rather than treating the cell as a lumped system. This spatial resolution becomes particularly significant during transient operation, when the cell transitions between endothermic and exothermic regimes and non uniform temperature profiles develop along the flow path.

Heat exchange between the gas channels and the solid cell is accounted for within each segment via the convective term in the energy equation. In addition, heat is transferred between adjacent cell and interconnector layers by solid state conduction, with the thermal resistance of each layer determined by its thickness and thermal conductivity. This conduction coupling ensures that the temperature of the solid structure evolves consistently with the thermal state of both gas channels.

The gas composition at each segment is determined by the local electrochemical reaction rate. Because oxygen ions produced at the cathode electrode are transported through the electrolyte and consumed at the anode electrode within the same segment, the mass conservation equations of the cathode and anode channels are coupled through the oxygen ion flux. As a result, changes in local current density directly affect the species concentrations on both sides of the cell at the same spatial location.

The cathode and anode gas flows are arranged in a cross flow configuration, meaning the two streams flow in perpendicular directions across the cell plane. This geometry causes the local current density and temperature to vary in two dimensions, since the gas composition and temperature along each channel depend on the position along that flow direction. The governing equations are therefore solved at each node of the two-dimensional spatial grid formed by the intersection of the cathode and anode flow directions.

The segmented model enables analysis of temperature gradients across the cell, which are a key indicator of thermal stress and degradation risk during transient load changes.

2.3. Simulation cases

To compare the dynamic behavior of the Steam–Air and Steam–Steam configurations, a reference operating condition is first established, and three simulation cases are defined based on it.

The reference condition is set at a current density of 1 A/cm2, with an inlet-to-outlet temperature difference of 50°C and a cathode inlet composition of H_2:H_2O = 0.2:0.8 (mole fraction). The steam utilization at the cathode is fixed at 80% at the reference current density of 1 A/cm^2. Based on these conditions, the corresponding anode side supply flow rates are calculated for each configuration. The reference flow rates used throughout the study are summarized in Table 2.

Table 2. *Reference operating conditions and supply flow rates.*

Parameter	Value
Current density [A/cm^2]	1
Inlet-outlet temperature difference [°C]	50
Cathode inlet composition (H_2 : H_2O)	0.2 : 0.8
Steam utilization [%] (@ 1A/cm^2)	80
Reference air flow rate [mol/s]	Air-Steam : 0.00267 Steam-Steam : 0.00137

Three simulation cases are defined to investigate distinct aspects of the dynamic behavior, as described below.

In Case 1, a voltage ramp input is applied to both configurations while the anode supply flow rate is held constant at the reference value. The voltage is increased from the open circuit voltage up to the level corresponding to the reference current density of 1 A/cm^2. This case captures the transient response of the cell temperature and current density as the operating point passes through the endothermic, thermoneutral, and exothermic regimes during a load increase.

In Case 2, the current density is fixed at the reference value of 1 A/cm^2 and the anode supply flow rate is varied stepwise by ±30% from the reference flow rate. This case isolates the effect of anode flow rate on the steady state and transient thermal behavior at a fixed electrochemical operating point, allowing direct comparison of the temperature and species distribution sensitivity between the two configurations.

In Case 3, the applied voltage is fixed at 1.1 V, which corresponds to an endothermic operating condition below the thermoneutral voltage, and the anode supply flow rate is again varied by ±30% from the reference value. This case examines how each configuration responds to changes in sweep gas flow rate under conditions where the cell continuously absorbs heat from the gas stream, which represents a thermally challenging regime for temperature control.

3. Results

Fig. 2 shows the dynamic responses of both configurations to a linearly increasing voltage input. The upper panel presents the applied voltage and the resulting current density, and the lower panel shows the outlet gas temperatures at the anode and cathode exits. The anode supply flow rates are held constant at the respective reference values throughout.

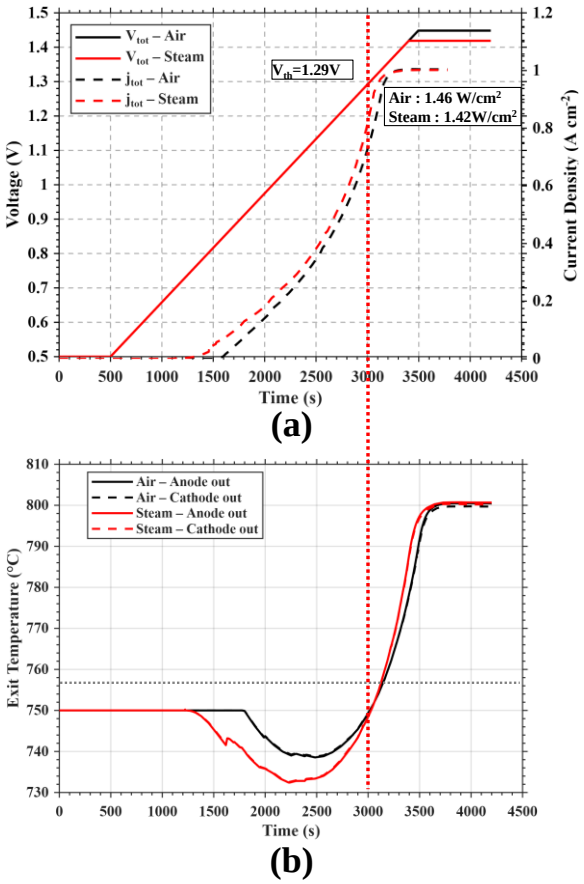

Figure.2. *(a) Dynamic response to a voltage ramp input. Applied voltage and current density for Steam–Air and Steam–Steam configurations. (b) Outlet gas temperatures at the anode and cathode exits of both configurations.*

The voltage ramp is applied from the open circuit voltage (OCV) and increased linearly until the target current density of 1 A/cm^2 is reached, after which the voltage is held constant. Current begins to flow once the applied voltage exceeds the OCV of each configuration. Notably, the Steam–Steam configuration reaches a given current density at a lower applied voltage than the Steam–Air configuration throughout the ramp. This is because the anode oxygen partial pressure is lower in the Steam–Steam case, where no nitrogen is present and the anode channel initially contains only steam. The lower oxygen partial pressure reduces the Nernst potential, which directly lowers the reversible voltage required to drive the electrolysis reaction. As a result, at the final operating point of 1 A/cm^2, the power density of the Steam–Air configuration is 1.46 W/cm^2, while the Steam–Steam configuration requires only 1.42 W/cm^2, a reduction of approximately 2.7%. Although this difference is modest, it reflects a consistent advantage of the Steam–Steam configuration in terms of cell level electrical efficiency.

Both configurations converge to the same current density of 1 A/cm^2 at the end of the ramp, as the reference anode flow rates are maintained unchanged and the voltage is held at the corresponding steady state level. The outlet temperatures of both configurations likewise converge to 800°C at steady state.

The outlet temperature responses in the lower panel of Fig. 2 exhibit a characteristic three stage profile that reflects the thermal regimes encountered during the ramp. In the initial phase, as the current density begins to rise, the endothermic reaction absorbs heat from the gas stream and the outlet temperatures drop below the inlet supply temperature of 750°C. As the voltage continues to increase and approaches the thermoneutral voltage of V_{th} = 1.29 V, the heat generated by the electrochemical irreversibilities exactly compensates the endothermic reaction enthalpy, and the outlet temperatures return to the supply gas temperature. Beyond the thermoneutral point, the exothermic regime takes over and the outlet temperatures rise continuously until reaching the steady state value of 800°C.

The Steam–Steam configuration shows a more pronounced temperature excursion compared to the Steam–Air configuration across both the endothermic and exothermic phases. This difference is directly attributable to the difference in heat capacity rate of the anode supply gas between the two configurations. As shown in Table 3, although steam has a higher molar heat capacity (Cp = 41.586 kJ/kmolK) than air (Cp = 33.175 kJ/kmolK), the reference molar flow rate of steam (1.37×10^{-3} mol/s) is substantially lower than that of air (2.267×10^{-3} mol/s). The resulting heat capacity rate of the steam supply is 0.0570 W/K, compared to 0.0752 W/K for air. Because the Steam–Steam anode stream carries less thermal capacity per unit time, the same heat flux from the endothermic reaction produces a larger temperature drop. In the endothermic phase, the minimum outlet temperature of the Steam–Steam configuration falls to approximately 733°C, compared to approximately 738°C for the Steam–Air configuration. In the exothermic phase, the lower heat capacity rate of steam similarly causes the outlet temperature to rise more rapidly once the thermoneutral point is passed, as the same amount of heat generation produces a greater temperature increase in the lower capacity stream.

Table 2. *Thermal characteristics of supplied steam and air*

Species	Steam (H_2O)	Air (N_2, O_2)
Molar flow rate [mol/s]	1.37×10^{-3}	2.267×10^{-3}
Cp @ 750°C [kJ/kmolK]	41.586	33.175
Heat capacity rate [W/K]	0.0570	0.0752

In Case 2, the current density is held constant at the reference value of 1 A/cm^2 and the anode supply flow rate is varied stepwise between +30% and −30% of the reference value. Fig. 3 shows the applied flow rate variation scenario. Starting from the reference flow rate, a step increases to +30% is applied at t = 500 s and maintained until t = 1100 s, followed by a step decrease to −30% at t = 1100 s held until t = 1700 s, after which the flow rate returns to the reference level.

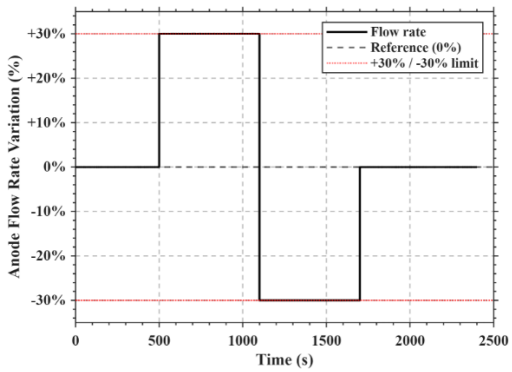

Figure. 3. *Anode inlet flow rate variation scenario for Case 2. The flow rate is varied stepwise from the reference (0%) to +30% and then to −30%.*

Fig. 4 shows the current density of each segmented cell as a function of time for the Steam–Air (left) and Steam–Steam (right) configurations. Each colored line corresponds to a different cell segment numbered from j1 (blue, anode inlet side) to j25 (red, anode outlet side), and the spread of these lines at any instant reflects the spatial non-uniformity of current density across the cell.

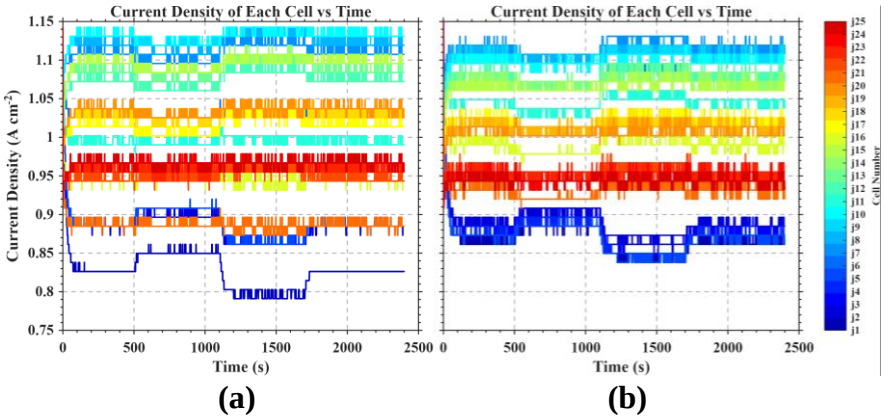

Figure. 4. *Current density of each segmented cell versus time for the (a) Steam–Air and (b) Steam–Steam configurations under Case 2 flow rate variation.*

At the reference flow rate, a clear spread exists between the cell segments, with j1 consistently lower and j25 higher than the cell average, reflecting the temperature gradient established by the cross-flow exothermic operation. When the flow rate is increased to +30% at t = 500 s, the additional thermal mass of the anode gas suppresses the temperature rise along the anode channel, resulting in a more uniform temperature distribution across the cell. This is directly reflected in the narrowing of the current density band: the high-current cells (j25 region) decrease slightly, and the low-current cells (j1 region) increase, reducing the overall non-uniformity. Conversely, when the flow rate is reduced to −30% at t = 1100 s, the reduced thermal capacity of the anode stream allows the exothermic heat to produce a steeper temperature gradient along the flow direction. The current density spread widens significantly, with j1 dropping to approximately 0.80 A/cm^2 while the high cells remain above 1.10 A/cm^2. After the flow rate returns to the reference level at t = 1700 s, the distribution recovers to its original state. Both the Steam–Air and Steam–Steam configurations exhibit qualitatively the same flow-rate sensitivity, confirming that the mechanism—anode-side thermal buffering—operates identically regardless of the sweep gas species. However, owing to the lower heat capacity rate of steam compared to air (0.0570 vs. 0.0752 W/K, Table 3), the temperature response in the Steam–Steam configuration is faster and somewhat more sensitive to flow rate changes, producing marginally larger transient excursions in the cell segment current densities during the flow rate step transitions.

Fig. 5 presents the two-dimensional current density distribution maps at steady state for each flow rate condition: the reference state at t ≈ 500 s, the +30% state at t ≈ 1100 s, and the −30% state at t ≈ 1700 s. The top row corresponds to the Steam–Air configuration and the bottom row to Steam–Steam. In these maps, the anode gas flows from left to right, and the cathode steam flows from top to bottom.

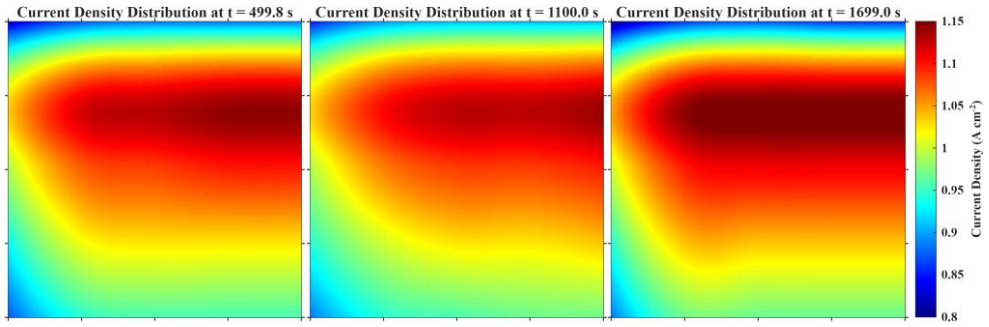

(a)

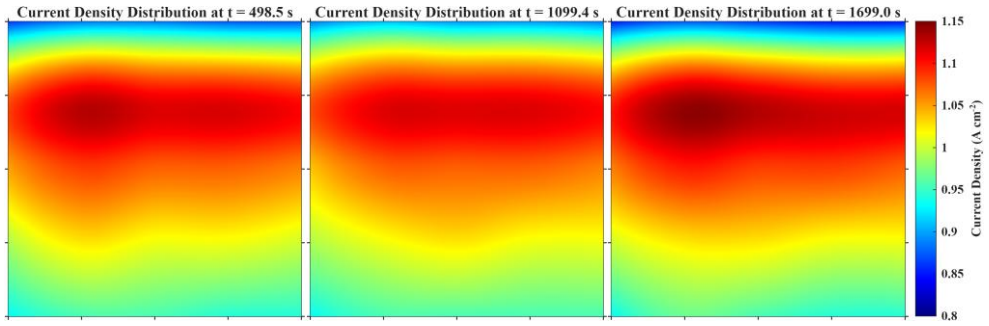

(b)

Figure. 5. *Steady-state current density distribution maps at t ≈ 500 s (reference), t ≈ 1100 s (+30% flow), and t ≈ 1700 s (−30% flow) for the (a) Steam–Air and (b) Steam–Steam configurations.*

Since the operating point is in the exothermic regime, heat accumulates progressively along both gas flow paths, causing the cell temperature—and with it the local current density—to increase toward the lower-right region of the map, where both the cathode steam and the anode gas are near their respective outlets. However, the peak current density does not occur at the very top of the cell but rather at a position slightly below the cathode inlet. At the cathode inlet (top edge), the incoming steam concentration is highest, which strongly promotes the electrochemical reaction; however, the temperature at this location is lowest because the fresh cathode gas has not yet been heated by the exothermic reaction. As the gas travels a short distance downward from the inlet, the cell temperature rises rapidly due to the heat released by the reaction, while the steam concentration remains high. The combination of elevated temperature and high steam concentration at this near-inlet region produces the highest local current density in the cell. Further toward the cathode outlet (bottom), the steam is progressively consumed and the driving concentration decreases, causing the current density to fall despite the continued temperature increase.

As the flow rate increases to +30%, the stronger thermal buffering of the anode gas moderates the temperature gradient across the cell. The hot spot in the lower-right region becomes less pronounced, the high-current-density peak broadens, and the minimum current density near the anode inlet rises. The overall distribution becomes more uniform. The opposite is observed at −30% flow: the weaker thermal buffering allows a steeper temperature gradient to develop, intensifying the hot spot at the lower-right and the cold spot near the anode inlet.

It is noted that the distribution maps in Fig. 5 are generated by internal interpolation of the discrete segment values for visualization purposes. The absolute values at individual spatial points should therefore be interpreted as indicative of the overall distribution trend rather than as precise pointwise results.

In Case 3, the applied voltage is fixed at 1.1 V, which corresponds to an endothermic operating condition below the thermoneutral voltage of V_{th} = 1.29 V. The anode supply flow rate is varied using the same stepwise scenario as in Case 2 (Fig. 3), with a +30% increase at t = 500 s followed by a −30% decrease at t = 1100 s and a return to the reference level at t = 1700 s.

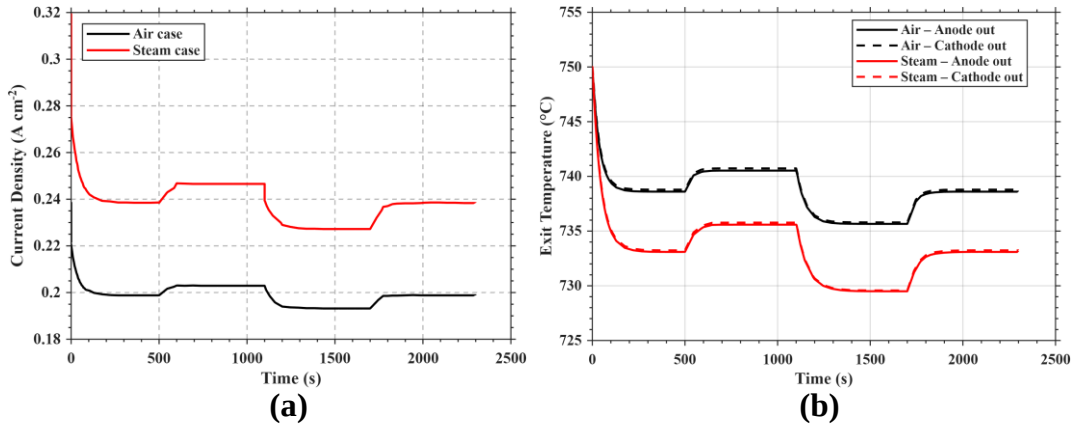

Figure. 6. *Dynamic responses to anode flow rate variation at a fixed voltage of 1.1 V. (a) Current density for Steam–Air and Steam–Steam configurations. (b) Anode and cathode outlet temperatures for both configurations.*

Fig. 6 shows the time evolution of the current density (left) and the outlet temperatures (right) under the Case 3 scenario. The most immediate observation is that, despite being operated at the same applied voltage of 1.1 V, the Steam–Steam configuration maintains a consistently higher current density than the Steam–Air configuration throughout the simulation: approximately 0.240 A/cm^2 for Steam–Steam compared to 0.200 A/cm^2 for Steam–Air at the reference flow rate. This difference arises from the lower open-circuit voltage (OCV) of the Steam–Steam configuration, which results from the reduced anode oxygen partial pressure. At a fixed applied voltage, a lower OCV translates directly into a larger electrochemical driving force, enabling a higher current density. Correspondingly, the Steam–Steam outlet temperature at steady state is approximately 733°C, which is about 6°C lower than the approximately 739°C observed for Steam–Air. The lower temperature in the Steam–Steam case is a direct consequence of the higher electrochemical reaction rate, which absorbs more heat from the gas stream through the endothermic reaction.

The dynamic response to each flow rate step confirms that the thermal behavior in the endothermic regime is qualitatively the opposite of that observed in Case 2. In the exothermic Case 2, a higher anode flow rate reduced the cell temperature by buffering the exothermic heat release. In the endothermic Case 3, a higher flow rate supplies more sensible heat to the cell from the incoming gas, raising the cell temperature and thereby increasing the current density. Conversely, a reduction in flow rate diminishes the heat supply, causing the cell temperature to fall and the current density to decrease accordingly. The current density thus follows the temperature response directly, reflecting the strong coupling between local temperature and electrochemical performance through both the activation energy of the electrode reactions and the ionic conductivity of the electrolyte.

The transient response times of the two configurations following each flow rate step are comparable, consistent with the design intent of matching the anode-side heat capacity rates between the two configurations. Both configurations reach the new steady state at approximately the same rate after each step change, and the magnitude of the temperature excursion per unit flow rate change is similar. The current density variation between the +30% and −30% conditions amounts to approximately 0.01 A/cm^2 for both configurations—a relatively modest range of about 5% of the respective reference values—indicating that, although the thermal state is sensitive to flow rate changes in the endothermic regime, the absolute sensitivity per unit flow variation is moderate.

4. Conclusion

This study compared the dynamic behavior of Steam–Air and Steam–Steam SOEC configurations using a segmented two-dimensional dynamic model across three simulation cases: a voltage ramp, anode flow rate variation under exothermic operation, and anode flow rate variation under endothermic operation.

When the reference operating conditions are matched in terms of inlet-to-outlet temperature difference at the same current density, the anode-side heat capacity rates of the two configurations differ only modestly (0.0570 vs. 0.0752 W/K), and the overall dynamic characteristics are broadly similar. The primary distinction between

the two configurations originates from the lower anode oxygen partial pressure in the Steam–Steam case, which reduces the OCV and lowers the reversible voltage. This yields a 2.7% reduction in power density under fixed-current operation and a noticeably higher current density under fixed-voltage endothermic operation. These results confirm that the Steam–Steam configuration is a dynamically viable alternative to Steam–Air, offering a consistent efficiency advantage while maintaining comparable transient response characteristics.

Acknowledgments

This work was partly supported by Korea Institute of Energy Technology Evaluation and Planning(KETEP) grant funded by the Korea government(MCEE)(RS-2025-16066396, Development of a SOEC stack with steam supply to both electrodes for hydrogen and oxygen co-production) and Korea Institute of Energy Technology Evaluation and Planning(KETEP) grant funded by the Korea government(MCEE)(RS-2025-16063345, Multiscale Degradation Model and AI-Based Lifetime Estimation for High-Durabilty 5kW-Clas SOEC Stack Development).

Nomenclature

- N Number of moles in control volume, mol
- $\dot{\mathrm{N}}$ Molar rate of gas in control volume, mol/s
- A Active reaction area, m^2
- j Current density, A/cm^2
- F Faraday constant, 96485 C/mol
- E Total energy in control volume, J
- q Enthalpy of gases, J
- $\dot{\mathrm{q}}$ Enthalpy rate of gas in control volume, J/s
- k Heat transfer coefficient, W/m^2K
- T Temperature, °C
- r Reaction rate per unit area, mol/m^2s
- e Specific enthalpy of gas, J/mol
- U Potential of cell, V
- η Over potential of cell, V
- R Gas constant, 8.314 J/molK
- p Partial pressure, Pa
- P Pressure, Pa
- n Molar ratio of reactants and electrons in a reaction, -

References

[1] International Energy Agency., World Energy Outlook 2025, IEA, Paris, 2025; https://iea.li/WEO2025

[2] T. Bui, D. Lee, K. Y. Ahn, Y. S. Kim., Techno-economic analysis of high-power solid oxide electrolysis cell system. Energy Conversion and Management, 2023; 278, 116704. https://doi.org/10.1016/j.enconman.2023.116704

[3] Y. Sun, T. Qian, J. Zhu, N. Zheng, Y. Han, G. Xiao, M. Ni, H. Xu., Dynamic simulation of a reversible solid oxide cell system for efficient H2 production and power generation., Energy, 2023; 263, 125725. https://doi.org/10.1016/j.energy.2022.125725

[4] L. Barelli, G. Bidini, G. Cinti. Steam as sweep gas in SOE oxygen electrode., Journal of Energy Storage, 2018, 20, 190–195. https://doi.org/10.1016/j.est.2018.09.014

[5] G. Min, Y. J. Park, J. Hong. Parametric analysis of solid oxide co-electrolysis cell systems: relationship between system performance, external heat and parasitic power., ECS Transactions, 2019; 91 (1), 207–214. https://doi.org/10.1149/09101.0207ecst

[6] A. Saeedmanesh, P. Colombo, D. McLarty, J. Brouwer., Dynamic behavior of a solid oxide steam electrolyzer system using transient photovoltaic generated power for renewable hydrogen production., Journal of Electrochemical Energy Conversion and Storage, 2019; https://doi.org/10.1115/1.4043340

[7] D. S. Wendt, L. T. Knighton, R. D. Boardman., High-Temperature Steam Electrolysis Process Performance and Cost Estimates. INL/RPT-22-66117. Idaho National Laboratory, 2022.

[8] D. Lee, T. Q. Quach, T. P. Israel, K. Y. Ahn, Y. Bae, Y. S. Kim., Development and analysis of a dynamic model for SOEC system. Proceedings of ECOS 2023